Images Constructed from Computed Flowfields

Leslie A. Yates*

Eloret Institute, Palo Alto, California 94303

A method for constructing interferograms, schlieren, and shadowgraphs from ideal- and real-gas, two- and three-dimensional computed flowfields is described. The computational grids can be structured or unstructured, and multiple grids are an option. The constructed images are compared with experimental images for several types of flow, including a ramp, a blunt body, a nozzle, and a reacting flow. The constructed images simulate the features observed in the experimental images. They are sensitive to errors in the flowfield solutions and can be used to identify solution errors. In addition, techniques for obtaining phase shifts from experimental finite fringe interferograms and for removing experimentally induced phase-shift errors are discussed. Both the constructed images and calculated phase shifts can be used for validation of computational fluid dynamics (CFD) codes.

Introduction

FOR decades experimental interferograms, schlieren, and shadowgraphs have been used for quantitative and qualitative flowfield studies. These three images are created by passing light through the flowfield, and the recorded intensity patterns are functions of the phase shift and angular deflection of the light.

In infinite and finite fringe interferograms, the recorded intensity patterns (fringes) are caused by phase shifts (optical path length differences). These phase shifts result from variations in the flowfield density and are proportional to path integrals of the refractive index. The path of integration is the path that the light follows through the flowfield.

For two-dimensional and axisymmetric flowfields, point information can be extracted from interferograms and compared with computational results. The first step in extracting this information is to calculate the phase shifts from the interferogram's fringe patterns. These phase shifts can be obtained from either infinite or finite fringe interferograms. However, in flowfield regions where there are only small changes in the density and, hence, fractions of fringe shifts, calculating the phase shifts from finite fringe interferograms will give more accurate results.

Several methods for calculating the phase shifts from finite fringe interferograms exist. These methods involve either tracing individual fringes,[1,2] fitting sinusoidal functions to intensity variations in a single interferogram,[3] or using multiple interferograms and phase-stepping techniques.[4] After the phase shifts are found, a transformation is applied, and the refractive index (as well as density for nonreacting flows) at every point in the flowfield is obtained. This point information can then be compared with flowfield solutions.

For three-dimensional flows, the transformation from the experimental phase shifts to point information cannot be made, and other methods of comparison must be used. For example, Strike et al.[5] presented theoretical interferograms over 15 years ago, Watkins[6] used path-averaged density contours to compare flowfield solutions with experimental infinite fringe interferograms, and Havener and Obergefell[7] tracked individual fringes through flowfield solutions and compared these results with experimental finite fringe interferograms. These methods do allow for comparison of computed and experimental flowfields but not necessarily on a one-to-one basis. A graphics package that was developed by Tamura and Fujii[8] and is available in Japan does have the capability of constructing interferograms, as well as schlieren and shadowgraphs, from computed flowfields. With this package, one-to-one comparisons of computation and experiment are possible.

In schlieren and shadowgraphs, the intensity patterns (dark and light regions) are governed by the angular deflection of the light as it passes through the flowfield. The angular deflection is proportional to the path integral of the refractive-index gradient. Flowfield features that have large refractive-index (density) gradients, such as shocks, shear layers, and expansion fans, are recorded in these images.

Both schlieren and shadowgraphs are used for flow visualization studies and for locating flowfield structures. Schlieren contain sharp details of the flowfield structures as well as information about the direction of the light when it exits the flow. Shadowgraphs also contain details of the flowfield. However, they contain no information about the direction of the light and are generally less sharp than schlieren. When these images are compared with computed flowfields, contour plots for only one plane of data (usually the symmetry plane) are typically used. The choice of contour levels can mask some of the features observed in the experimental images. In addition, if the flow is three-dimensional or the model is free to roll, no single computational plane provides all of the information necessary for realistic comparisons to experimental images.

The information required for constructing interferograms, schlieren, and shadowgraphs is contained in the flowfield solutions. The refractive index is proportional to the gas-species densities, and these densities are always calculated in the solutions. By developing routines to evaluate and integrate appropriate functions of the refractive index, direct comparisons of computed and experimental results can be made.

In this paper, the constructed interferograms, schlieren, and shadowgraphs (CISS) code is described. CISS is software that constructs images from ideal- and real-gas, two-dimensional, axisymmetric, and three-dimensional computed flowfield solutions. The computational grids can be structured or unstructured, and multiple grids are an option. This software differs from that of Tamura and Fujii[8] in that with CISS the computational cells are not divided into tetrahedra; CPU time requirements are reduced by eliminating the need for ray tracing; all image points are calculated, and no interpolation between image points is required; the integration arguments are functions of the refractive index, not the density, and images for real-gas flows can easily be constructed; and the method for constructing shadowgraphs is different. Constructed and experimental images are shown for several types of flowfields, and the effects of grid resolution and solution convergence are discussed.

In any comparison of experimental and constructed images, the issue of optical aberrations should be addressed. These aberrations must be determined individually for each experiment, and they should be removed from the experimental image before comparisons between experiment and computation are made. Although a

general treatment of this subject is beyond the scope of this paper, an experimental finite fringe interferogram is used to demonstrate the importance of identifying and removing aberrations. In this example, a method for extracting phase-shift information from the experimental interferogram is described. The phase-shift errors that are caused by optical aberrations are then identified and removed from the calculated phase shifts.

Constructing Images

The construction of interferograms, schlieren, and shadowgraphs from flowfield solutions requires three steps: 1) identifying and evaluating the appropriate functions of the refractive index, 2) integrating these functions along lines of sight, and 3) postprocessing the integrals to give the desired images. In this section, these three processes are described, and estimations of the errors introduced in the construction of these images are presented.

Refractive-Index Functions

Excellent discussions of the types of images that can be created by passing light through a flowfield and the theory that describes the resulting intensity patterns are available in various texts and papers (e.g., Refs. 9 and 10). However, since codes that create these images from computed flowfields are useful to scientists and engineers with diverse backgrounds, a summary is included here for completeness.

As light passes through a flowfield, its phase and direction are changed. The changes can be obtained by integrating functions of the refractive index along lines of sight. For ideal and nonreacting gases, the refractive index n is simply

$$n = 1 + \kappa \rho$$

where κ is the appropriate Gladstone-Dale constant for the gas, and ρ is the density. For both equilibrium and nonequilibrium real-gas solutions, the species mass fractions vary throughout the flow, and the refractive index is given by the sum of the contribution from each gas,[3]

$$n = 1 + \sum_i \kappa_i \rho_i$$

The Gladstone-Dale constant for the ith species is κ_i, and the partial density is ρ_i.

Interferograms are created by exposing the film to two laser beams: the reference beam and the object beam. The reference beam does not pass through the flowfield, and its phase is unchanged. The object beam does pass through the flowfield, and its phase is changed by variations in the refractive index (density). The fringe patterns recorded in the interferogram result from the interference of these two light beams. When calculating interferograms from computed flowfields, the phase shift of the object beam relative to the reference beam is obtained by integrating

$$f(n) = \frac{2\pi}{\lambda} (n - n_0)$$

along a line of sight. Here, n_0 is the refractive index of the undisturbed flow and λ is the wavelength of the light.

Schlieren are created by passing collimated light through the flowfield, focusing this light to a point, using a knife edge to block out a portion of the light, and then refocusing the remaining light
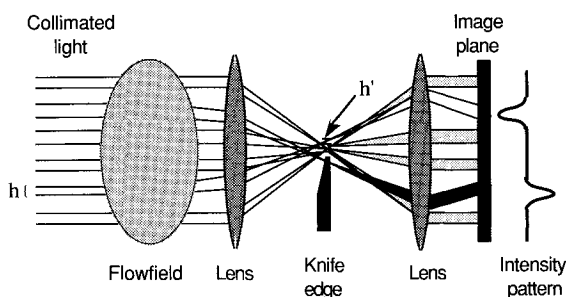

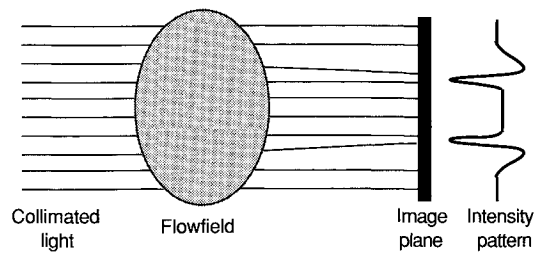Fig. 1 Schematic for constructing schlieren.

Fig. 2 Schematic for constructing shadowgraphs.

onto an image plane (Fig. 1). The amount of light blocked by the knife edge is proportional to the angular deflection of the light; the angular deflection is proportional to the refractive-index (density) gradient. The incremental change in the angular deflection at any point in the flowfield is

$$\delta\varepsilon_x = f(n) = \frac{1}{n}\frac{\partial n}{\partial x} \quad \text{and} \quad \delta\varepsilon_y = f(n) = \frac{1}{n}\frac{\partial n}{\partial y}$$

Integrating these functions along a line of sight gives the total angular deflections ε_x and ε_y.

In shadowgraphs, no knife edge is used, and the dark and light regions are caused by the concentration and divergence of light (Fig. 2). In many texts (e.g., Refs. 9 and 10), the function used to describe shadowgraphs is the line integral of the second derivative of the refractive index. In CISS, the function of the refractive index used for constructing shadowgraphs has been chosen to be equal to that used for schlieren. At the exit of the computed flowfield, the angular deflection is known. If the distance to the image plane is also known, then the area on the image plane where the deflected light falls is known, and the shadowgraph can be constructed by adding the contribution of the deflected light beams at each point on the image plane. It should be noted that if

$$\frac{\partial\varepsilon_x}{\partial x} + \frac{\partial\varepsilon_y}{\partial y} = \frac{\partial}{\partial x}\int\frac{1}{n}\frac{\partial n}{\partial x}\,ds + \frac{\partial}{\partial y}\int\frac{1}{n}\frac{\partial n}{\partial y}\,ds = 0$$

there will be no convergence or divergence of the light and, hence, no variation in shade. The form of this equation provides the motivation for describing shadowgraphs as line integrals of the second derivative, although this description is not precisely correct. Tamura and Fujii[8] constructed shadowgraphs by calculating the divergence ($\nabla \cdot$) of the integrated density gradient. In CISS the light is actually projected onto the image plane. The advantage of constructing shadowgraphs in this manner is that the thickness of the dark and bright regions can be controlled by the placement of the image plane. This dependency of the dark and bright regions on the image plane's position is observed in experimental shadowgraphs.

Integration Scheme

The intensity variations observed in the images are governed by integrals of the refractive-index functions described in the preceding section. If an image is divided into an $M \times N$ array of pixels, these integrals must be evaluated for every pixel in the image. The integral for the (m, n)th element of the array is

$$F_{m,n} = \int_0^z f\{n[x_m(\zeta), y_n(\zeta), \zeta]\}\frac{ds}{d\zeta}\,d\zeta$$

where ds is the element of arc length. The light's path, defined by $[x_m(\zeta), y_n(\zeta), \zeta]$ for $0 \leq \zeta \leq z$, intersects the image plane at the (m, n)th element. This integral can be written as

$$F_{m,n} = \sum_{i=1}^N \int_{Z_i}^{Z_{i+1}} f\{n[x_m(\zeta), y_n(\zeta), \zeta]\}\frac{ds}{d\zeta}\,d\zeta$$
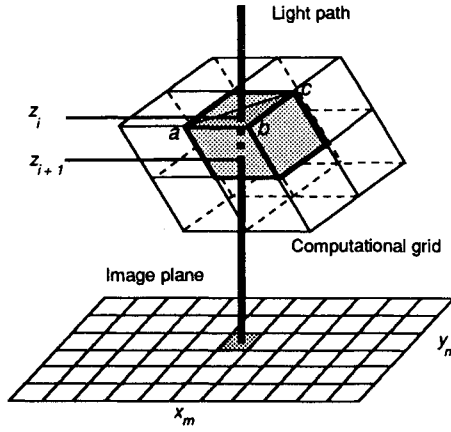
Fig. 3 Schematic for the integration process.

where the i summation is over all computational cells that contain segments of the line of integration. The interval $z_i \le \zeta \le z_{i+1}$ defines the intersection of the line of integration with the ith computational cell (Fig. 3).

Tracing the actual light path as it bends through the flowfield solution and integrating the appropriate function of the refractive index along this path is computationally expensive. The computer resources required for producing constructed images can be appreciably reduced by approximating the light's path by a straight line perpendicular to the image plane. With a straight line approximation, x_m and y_n become independent of ζ, and $F_{m,n}$ can be rewritten as

$$F_{m,n} = \sum_{i=1}^{N} \int_{z_i}^{z_{i+1}} f[n(x_m, y_n, \zeta)] \, d\zeta$$

The order of evaluation and summation of the integrals has no effect on $F_{m,n}$, and, therefore, no ray tracing is required. It is necessary only to find the intersection of the line of integration with each computational cell, calculate the integral for this segment, and add it to the appropriate sum.

To determine whether the line of integration intersects the computational cell, it is necessary to determine if the point (x_m, y_n, ζ) falls within the computational cell for any value of ζ. In CISS, the test procedure is as follows. Each computational cell (for example, the cell shaded in gray in Fig. 3) is defined by eight points and six surfaces. Each surface is then described by two triangles, and for each triangle, three cross products are formed:

$$(x_a - x_{mn}) \times (x_a - x_b)$$

$$(x_b - x_{mn}) \times (x_b - x_c)$$

$$(x_c - x_{mn}) \times (x_c - x_a)$$

In these equations, $x_{mn} = (x_m, y_n, z)$ gives the position of the (m, n)th pixel of the image array, and the $x_i = (x_i, y_i, z)$ for $i = a$, b, and c are the projections onto the image plane of the vectors that define the vertices of the triangle. To minimize CPU time, testing is performed only for x_m and y_n that lie within the minimum and maximum x and y values for the computational cell. The sign for all three cross products is the same if and only if the point lies within the triangle, and the triangular surfaces through which the line of integration enters and exits the computational cell can be determined. Once these surfaces are determined, interpolated values for z_i, z_{i+1}, $f(x_m, y_n, z_i)$, and $f(x_m, y_n, z_{i+1})$ are obtained, and the line integral of the function is evaluated using the trapezoidal rule. In CISS, three functions of the refractive index are integrated simultaneously: $n - n_0$, $(1/n) \, \partial n / \partial x$, and $(1/n) \, \partial n / \partial y$.

Combining this searching routine with the straight line approximation minimizes the CPU time required for creating the images. For regions of the flow without shocks, the straight line approximation should have a minimal effect on the constructed images. In shock regions, the refractive index changes rapidly, and the approximation may introduce errors; however, these errors are in many cases on the order of, or smaller than, the solution and experimental errors.

Estimation of Errors

The constructed images have several sources of errors. These include errors in the flowfield solutions, the approximation of the light path by a straight line, the interpolation schemes, and the accuracy of the integration method. Although solution errors are of great importance, they will be mentioned in this paper only when they directly affect the process of constructing images from flowfield solutions.

The error E introduced by the straight line approximation can be written as

$$E = \int f[x(\zeta), y(\zeta), \zeta] \, ds - \int f(0, 0, \zeta) \, d\zeta$$

$$= \int f[x(\zeta), y(\zeta), \zeta] \, (ds - d\zeta)$$

$$+ \int \{ f[x(\zeta), y(\zeta), (\zeta)] - f(0, 0, \zeta) \} \, d\zeta$$

For simplicity, the x and y coordinates of the image pixel have been set equal to zero. The first integral on the right-hand side of this equation represents the error introduced by the difference in path length; the second term represents the error introduced by approximating f by its value on the straight line. By writing the element ds as

$$ds = d\zeta \sqrt{1 + \left(\frac{dx}{dz} \Big|_{(x,y,\zeta)} \right)^2 + \left(\frac{dy}{dz} \Big|_{(x,y,\zeta)} \right)^2}$$

and by expanding the integrands in terms of f, x, y, dx/dz, and dy/dz, the expression for the error can be written as

$$E = \frac{1}{2} \int f(0, 0, \zeta) \left[\left(\frac{dx}{dz} \Big|_{(0,0,\zeta)} \right)^2 + \left(\frac{dy}{dz} \Big|_{(0,0,\zeta)} \right)^2 \right] d\zeta$$

$$+ \int \left[\frac{\partial f}{\partial x} \Big|_{(0,0,\zeta)} x + \frac{\partial f}{\partial y} \Big|_{(0,0,\zeta)} y \right] d\zeta + \cdots$$

If the light and integration paths initially coincide, $x \sim \int dx/dz \, d\zeta$ and $y \sim \int dy/dz \, d\zeta$. The derivatives dx/dz and dy/dz can be approximated by $\varepsilon_{x_0} + \int \kappa \partial \rho / \partial x \, d\zeta$ and $\varepsilon_{y_0} + \int \kappa \partial \rho / \partial y \, d\zeta$ where ε_{x_0} and ε_{y_0} are the initial angles between the light and integration path. Substituting these expressions into the previous equation gives

$$E = \frac{l}{2} \, f(\varepsilon_{x_0}^2 + \varepsilon_{y_0}^2) + \frac{l^2}{2} \left[\kappa f \left(\varepsilon_{x_0} \frac{\partial \rho}{\partial x} + \varepsilon_{y_0} \frac{\partial \rho}{\partial y} \right) \right.$$

$$+ \left. \left(\varepsilon_{x_0} \frac{\partial f}{\partial x} + \varepsilon_{y_0} \frac{\partial f}{\partial y} \right) \right] + \frac{l^3}{6} \left\{ \kappa^2 f \left[\left(\frac{\partial \rho}{\partial x} \right)^2 + \left(\frac{\partial \rho}{\partial y} \right)^2 \right] \right.$$

$$+ \left. \kappa \left(\frac{\partial f}{\partial x} \frac{\partial \rho}{\partial x} + \frac{\partial f}{\partial y} \frac{\partial \rho}{\partial y} \right) \right\}$$

where l is the length through the disturbed region of the flowfield.

For interferograms, the function f controls the phase shift and is given by $f = 2\pi (n - n_0) / \lambda = 2\pi\kappa (\rho - \rho_0) / \lambda$; λ is the wave-

length of the light used to create the interferogram. The estimated error in the calculated phase shift reduces to

$$\Delta\phi \approx \left(\frac{\pi\kappa(\rho-\rho_0)\,l}{\lambda}\right)(\varepsilon_{x_0}^2 + \varepsilon_{y_0}^2) + \frac{\pi\kappa l^2}{\lambda}\left\{[1+\kappa(\rho-\rho_0)]\right.$$

$$\times\left(\varepsilon_{x_0}\frac{\partial\rho}{\partial x} + \varepsilon_{y_0}\frac{\partial\rho}{\partial y}\right)\right\} + \frac{\pi\kappa^2 l^3}{3\lambda}\left\{[1+\kappa(\rho-\rho_0)]\right.$$

$$\times\left[\left(\frac{\partial\rho}{\partial x}\right)^2 + \left(\frac{\partial\rho}{\partial y}\right)^2\right]\right\}$$

Under most conditions, $\kappa\rho$ is much less than one, and the previous estimate can be manipulated to give $\mathcal{O}(\Delta\phi)$, the order of the error in the calculated phase shift:

$$\mathcal{O}(\Delta\phi) \sim \mathcal{O}\left\{\frac{\pi\kappa(\rho-\rho_0)\,l}{\lambda}(\varepsilon_{x_0}^2 + \varepsilon_{y_0}^2) + \frac{\pi\kappa^2 l^3}{3\lambda}\right.$$

$$\times\left[\left(\frac{\partial\rho}{\partial x}\right)^2 + \left(\frac{\partial\rho}{\partial y}\right)^2\right]\right\}$$

In schlieren and shadowgraphs, the light and dark regions are governed by the deflection of the light through the flowfield. The function that controls this deflection is proportional to the gradient normal to the light path of the refractive index (and hence the density). The order of the error in the calculated deflection angle ε_x is

$$\mathcal{O}(\Delta\varepsilon_x) \sim \mathcal{O}\left\{\frac{\kappa l}{2}\frac{\partial\rho}{\partial x}(\varepsilon_{x_0}^2 + \varepsilon_{y_0}^2) + \frac{\kappa l^2}{2}\left[\frac{\partial^2\rho}{\partial x^2}\left(\varepsilon_{x_0} + \frac{\kappa l}{3}\frac{\partial\rho}{\partial x}\right)\right.\right.$$

$$\left.+ \frac{\partial^2\rho}{\partial x\,\partial y}\left(\varepsilon_{y_0} + \frac{\kappa l}{3}\frac{\partial\rho}{\partial y}\right)\right] + \frac{\kappa^3 l^3}{6}\frac{\partial\rho}{\partial x}\left[\left(\frac{\partial\rho}{\partial x}\right)^2 + \left(\frac{\partial\rho}{\partial y}\right)^2\right]\right\}$$

A similar equation can be obtained for ε_y.

For all three images, the errors introduced by the straight line approximation are functions of the initial angle between the integration path and the actual light path. This initial angle, for instance, might be caused by the deflection of the light as it passes through an outer shock. To estimate this angle, consider light passing through a two-dimensional shock. The deflection angle ε_0 is given by

$$\varepsilon_0 = \sin^{-1}\left[\cos\theta\left(\sqrt{1-\left(\frac{n_1}{n_2}\right)^2\cos^2\theta} - \frac{n_1}{n_2}\sin\theta\right)\right]$$

The angles θ and ε_0 are defined in Fig. 4; n_1 and n_2 are the refractive indices on the incident and transmitted sides of the shock. The maximum deflection angle through the shock is

$$\varepsilon_0 = \sin^{-1}\left(\frac{n_2^2 - n_1^2}{n_2^2 - n_1^2}\right) \sim \kappa(\Delta\rho)$$
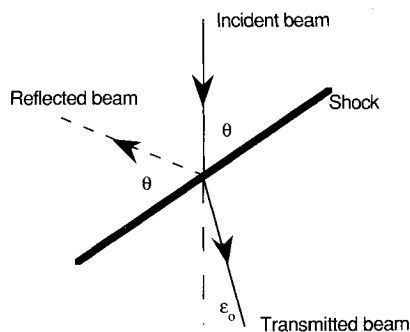

Fig. 4　Refraction of light through a shock.

where $\Delta\rho$ is the change in density through the shock, and the initial angles in the error estimates can be replaced by $\kappa\Delta\rho$.

The estimates on the order of the errors introduced by the straight line approximation are functions of the flowfield density, its derivative, and the Gladstone-Dale constant for the gas. For air, $\kappa\rho_{stp}$ is approximately 3×10^{-4} where ρ_{stp} is the density at standard room temperature and pressure. Normalizing the density ρ by ρ_{stp} allows the error estimates to be rewritten as

$$\mathcal{O}(\Delta\phi) \sim \mathcal{O}\left(\frac{1}{\lambda^*}\left\{10^{-10}(\rho^* - \rho_0^*)(\Delta\rho^*)^2 + 10^{-7}\right.\right.$$

$$\left.\left.\times\left[\left(\frac{\partial\rho^*}{\partial x^*}\right)^2 + \left(\frac{\partial\rho^*}{\partial y^*}\right)^2\right]\right\}\right)$$

and

$$\mathcal{O}(\Delta\varepsilon_x) \sim \mathcal{O}\left\{10^{-11}(\Delta\rho^*)^2\frac{\partial\rho^*}{\partial x^*} + 5\times10^{-8}\right.$$

$$\times\left[\frac{\partial^2\rho^*}{\partial x^{*2}}\left(\Delta\rho^* + \frac{1}{3}\frac{\partial\rho^*}{\partial x^*}\right) + \frac{\partial^2\rho^*}{\partial x^*\partial y^*}\left(\Delta\rho + \frac{1}{3}\frac{\partial\rho^*}{\partial y^*}\right)\right]$$

$$\left.+ 5\times10^{-12}\frac{\partial\rho^*}{\partial x^*}\left[\left(\frac{\partial\rho^*}{\partial x^*}\right)^2 + \left(\frac{\partial\rho^*}{\partial y^*}\right)^2\right]\right\}$$

In these expressions x, y, and λ have been nondimensionalized by l.

The wavelength of light used to create most interferograms is on the order of 4–7×10^{-7} m, and l/λ can be a large number. If l is on the order of meters, the order of the error in the calculated phase shift will be

$$\mathcal{O}(\Delta\phi) \sim \mathcal{O}\left\{10^{-3}(\rho^* - \rho_0^*)(\Delta\rho^*)^2\right.$$

$$\left.+ 3\times10^{-1}\left[\left(\frac{\partial\rho^*}{\partial x^*}\right)^2 + \left(\frac{\partial\rho^*}{\partial y^*}\right)^2\right]\right\}$$

For the straight line approximation to be valid for flows of a few meters, the density jumps must be less than 10 times the density at standard room temperature and pressure and the normalized density gradients in regions of the flow away from shocks must be less than one. It should be noted that if these conditions are violated, areas of the interferogram can still be accurate. These areas include regions where the light is nearly normal to the shock and where the light does not pass through regions of rapidly varying density. The schlieren and shadowgraphs will be accurate for a much wider range of conditions.

Two other sources of error are caused by inaccuracies in the interpolation and integration methods. As described earlier, the surfaces of the computational cell are triangulated, and the triangle through which the light beam enters or exits the computational cell is determined. A linear interpolation then uses values at the three vertices of the triangle to calculate the z coordinate, the refractive index, and the refractive-index gradient at the entrance or exit point. Once these values are calculated, the integral is found using the trapezoidal rule, a second-order method. Both the linear interpolation and the integration method can introduce errors. However, these errors are minimized when the grid has been adapted to the flowfield solution and large gradient regions are well resolved by the computational grid.

Construction of the Images

For infinite fringe interferograms, the intensity pattern is simply proportional to the sine of the phase shift ϕ:
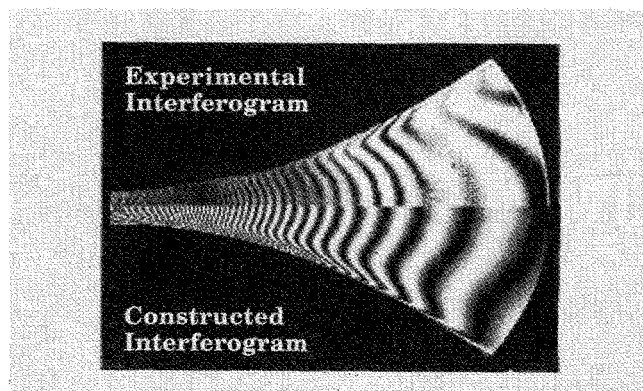
$$\phi = \frac{2\pi}{\lambda}\int_0^z (n-n_0)\,d\zeta$$

Fig. 5 Experimental and constructed infinite fringe interferograms for two-dimensional nozzle flow.[11]

For finite fringe interferograms, a linearly varying phase is added:

$$\delta\phi = k_x x + k_y y$$

where k_x and k_y are functions of the angle between the reference and object beams.

For schlieren, the intensity is a function of the angular deflection. As an example, consider a horizontal knife edge (Fig. 1) and a rectangular section of the initial light source with height h. As this rectangular section passes through the flowfield, it is deflected and exits the flowfield at an angle. When this light is focused at the plane of the knife edge, the rectangular element has a height of h' and has been deflected vertically by a distance $\gamma\varepsilon_y$; γ is a function of the distance between the flowfield and the knife edge. There is also a horizontal deflection; however, it is unimportant in this case. If the horizontal knife edge is placed at the center of the plane, the ratio of light not blocked by the knife edge to the amount of the original light is

$$0 \quad \text{for} \quad \frac{\gamma\varepsilon_y}{h'} \leq -\frac{1}{2}$$

$$1 \quad \text{for} \quad \frac{\gamma\varepsilon_y}{h'} \geq \frac{1}{2}$$

$$\frac{1}{2} + \frac{\gamma\,\varepsilon_y}{h'} \quad \text{for} \quad -\frac{1}{2} < \frac{\gamma\varepsilon_y}{h'} < \frac{1}{2}$$

and the intensity patterns are functions of this ratio.

As mentioned previously, shadowgraphs are not constructed in CISS from line integrals of second derivatives of the refractive index. Instead they are given by variations in intensity caused by the deflection of the light. In CISS it is assumed that the distance through the region of disturbed flow is much less than the distance to the image plane and that, whereas the deviation of the light path from a straight line path is not significant in this region, it is large enough to cause variations in intensity at the image plane. The shadowgraphs are constructed by tracking elements of light after they exit the disturbed flow region. The location and size of each light element is governed by four light rays that define the corners of that element, and the direction of these four light rays is given by the angle at which they exit the disturbed flow region; that is, shadowgraphs are also governed by ε_x and ε_y. Using these angles, the size and position of each light element at the image plane is calculated, and the amplitude of the electric field E_{mn} at the (m, n)th pixel in the image plane is increased by

$$\Delta E_{mn} = E_0 \left(\frac{C_f \cap A_{mn}}{C_i} \right)$$

where E_0 is the amplitude of the initial field, $C_f \cap A_{mn}$ is the area of the intersection of the deflected element with the (m, n)th pixel of the image plane, and C_i is the initial area of the deflected element. The intensity pattern observed in the shadowgraph is proportional to the square of E_{mn}.

The time requirements for constructing these images from flowfield solutions are linearly proportional to the grid size and the number of pixels defining the image. For two-dimensional flowfields, the image construction takes only a few seconds on a CRAY-YMP. For three-dimensional and axisymmetric flowfield solutions, more CPU time is required. For example, the construction of an image with 400,000 pixels from a flowfield solution with 250,000 grid points will take a few CPU minutes.

Examples of Constructed Images

Representative images are shown in this section for several types of hypersonic flows, including a nozzle, a blunt body, a ramp, and a reacting flow. The computed flowfields include two-dimensional, axisymmetric, and three-dimensional solutions. The purpose here is not to provide a detailed analysis of the computations but to simply demonstrate the ease of using constructed images for comparing experimental and computed results.

In Fig. 5, experimental and constructed infinite fringe interferograms are shown for a two-dimensional nozzle flow.[11] The experiment was performed in the Electric Arc Shock Tunnel at NASA Ames Research Center, and the test gas was nitrogen. The test conditions were such that nitrogen dissociation and recombination were important, and a real gas computational fluid dynamics (CFD) code was used for the flowfield solutions. Note that, by constructing an infinite fringe interferogram from the flowfield solution, one-to-one comparisons of computation and experiment are possible. The areas along the centerline where the experimental
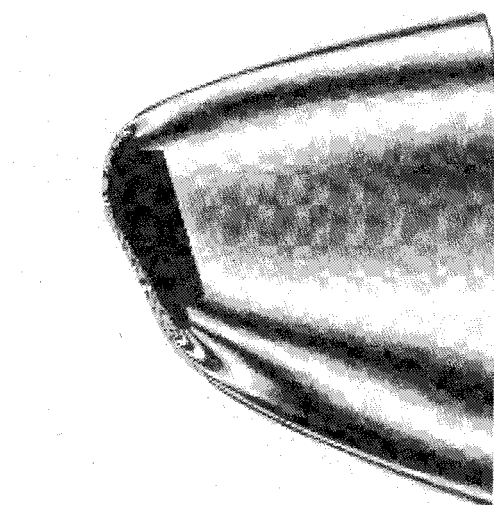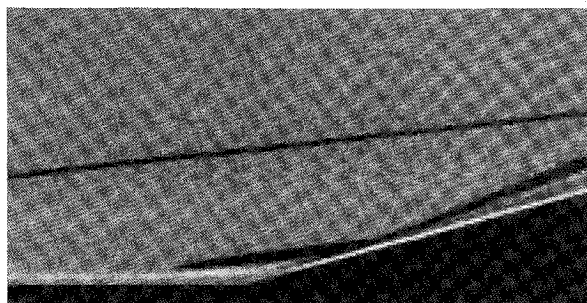

a)   **Constructed interferogram**

b)   **Experimental interferogram**

Fig. 6 Constructed and experimental infinite fringe interferograms for an AFE model. Three-dimensional flowfield solution: Venkatapathy et al.[12]; experiment performed at NASA Ames Research Center's ballistic range (unpublished data).

and computed densities agree or disagree easily can be seen by the matching (on the left-hand side of the interferogram) or mismatching (on the right) of the fringes. Differences between the computed and experimental boundary-layer thickness and the density near the wall are readily seen from the differences in the shapes and orientations of the individual fringes.

In Fig. 6, constructed and experimental infinite fringe interferograms are shown for a ballistic range test of the aeroassist flight experiment (AFE). The flowfield solution was calculated using an ideal-gas CFD solver;[12] the grid was adapted to the flowfield solution using SAGE.[13] A one-to-one comparison of the two interferograms is not possible; the flowfield solution is for a model with no yaw, and the experimental model did yaw. However, there are similarities. The constructed and experimental interferograms both show similar light and dark patterns, and the number of fringe shifts is comparable. The location of the fringes provides information as to the values of the computed and experimental integrated refractive indices.

In Fig. 7, constructed and experimental schlieren are shown for a two-dimensional, 15-deg compression corner; the flow is from left to right. The flowfield solution was computed using an ideal gas solver.[14] For both schlieren, a horizontal knife edge was used. The shocks, shear layers, and separation region observed in the

a)   Constructed schlieren
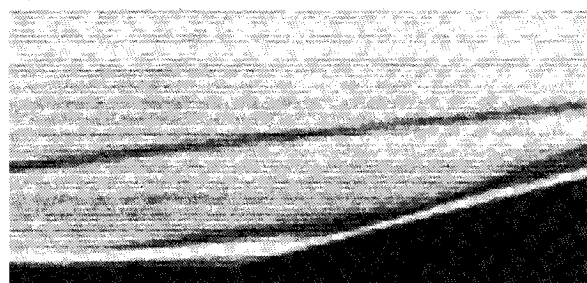

b)   Experimental interferogram

Fig. 7   Constructed and experimental schlieren for a two-dimensional compression ramp. Flow solution: Tokarcik et al.[14]; experiment: Delery and Coet.[15]

experimental schlieren[15] are simulated by the constructed schlieren. The dark regions in the constructed schlieren are caused by rapid increases in density across the computed shocks, and they correspond to dark regions in the experimental schlieren. The light regions in both the constructed and experimental schlieren are identified with boundary layers, and they are caused by density gradients near the surface. A shear layer (identified with a light region) lifts off the surface when separation occurs, and the extent of the computed and experimental separation regions can be compared. The grid for the computational study was not adapted to the flowfield solution. The sharpness of the features in the constructed schlieren could be further improved by using grid adaptation to reduce solution errors.
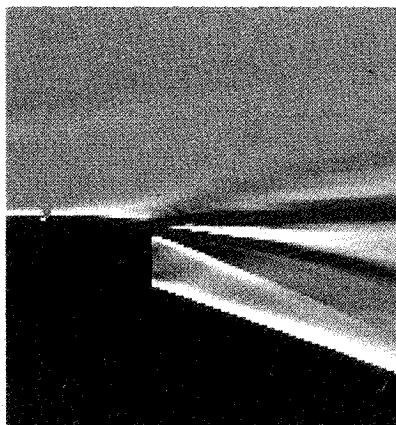
In Fig. 8, constructed and experimental shadowgraphs for a generic, National AeroSpace Plane (NASP) nozzle configuration, the single expansion ramp nozzle (SERN), are shown. Both the freestream and nozzle flows are supersonic. The flowfield solution in Fig. 8a is a two-dimensional, ideal gas solution at the symmetry plane; the solution in Fig. 8b is three-dimensional.[16] The interaction of the external flow with the nozzle plume is complicated, and all of the features observed in the experimental shadowgraph are captured in the constructed shadowgraphs. These features include the leading-edge shock, separation from the cowl, and the shocks, shear layers, and expansion fans caused by the interaction of the nozzle plume with the freestream. As with the schlieren, dark and light regions in the constructed shadowgraph correspond to dark and light regions in the experimental shadowgraph. However, whereas the shocks in the schlieren are described by either a single dark (or light) line, shocks in the shadowgraphs are described by a combination of dark and light lines. It should be noted that there are two parameters in CISS that allow the effective sensitivity and exposure of the film to be modeled. In this case, these parameters were chosen to emphasize the location of the flowfield features; they do not simulate the experimental film characteristics.

In the two constructed shadowgraphs in Fig. 8, the effects of grid resolution and solution errors can be seen. The grid in the two-dimensional solution is very fine, and the constructed shadowgraph resembles the experimental shadowgraph. For the three-dimensional solution, although multiple grids were used, the gridding was much coarser than that used for the two-dimensional solutions. The shocks, shear layers, and expansion fans were not as well resolved in the three-dimensional flowfield solution and, hence, are more diffuse in the constructed shadowgraph. The leading-edge shock in the three-dimensional computation has become so diffuse that it is barely detectable in the constructed shadowgraph.
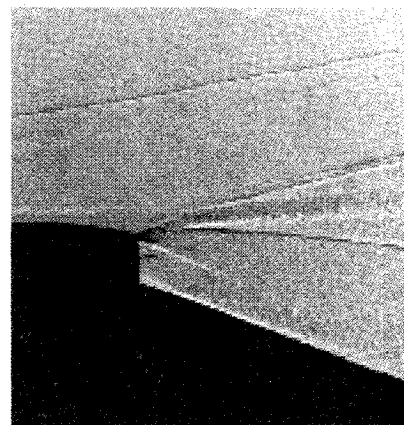
In Fig. 9, a constructed shadowgraph is shown for an axisymmetric, real-gas, flowfield solution of a ballistic range shot of a hemisphere cylinder into a combustible mixture.[17,18] Also shown is an experimental shadowgraph at slightly different test conditions.[19] This flow is very complex, and many of the features observed in the shadowgraph are three dimensional and difficult to
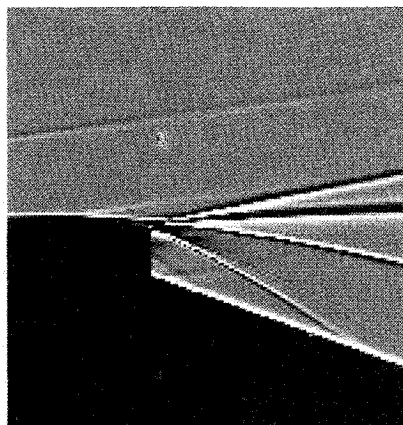
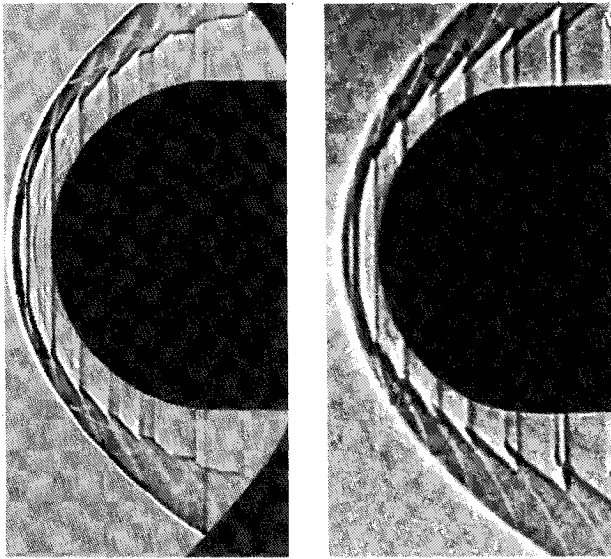a)   Constructed schlieren   b)   Three-dimensional solution   c)   Experiment

Fig. 8   Constructed and experimental shadowgraphs for SERN. Two-dimensional flow solution and experiment: Ruffin et al.[16]

a) Constructed shadowgraph   b) Experimental shadowgraph

Fig. 9 Constructed and experimental shadowgraphs for a hemisphere cylinder in a combustible mixture. Flowfield solution: Wilson[17] and Wilson and Sussman[18]; experiment: Lehr.[19]

identify in ordinary contour plots. In the constructed shadowgraph, most, if not all, of the features in the experimental shadowgraph are captured. It should be noted that in most shadowgraphs the leading edge of a shock is usually seen as a dark line immediately followed by a bright line. In this case, the optical setup of the experiment reversed the order of the dark and bright lines. CISS was able to duplicate this effect by using a negative number to represent the distance to the image plane, and a one-to-one comparison of experiment and computation is possible.

Interpreting Finite Fringe Interferograms

In the previous section, it has been demonstrated that the ability to construct images from computed flowfields facilitates the comparison of experiment and computation; hence, the CISS code provides a useful tool for CFD code validation. The capability for removing optical aberrations and for extracting fringe shift information from finite fringe interferograms is also invaluable for code validation. The interference patterns recorded in interferograms are functions of the phase shifts caused by variations in the refractive index. For low-density flows, there may be only fractions of fringe shifts in the regions of interest (for instance, the wake region), and the phase shifts cannot be determined from the fringe patterns in infinite fringe interferograms. However, they can be determined from the patterns in finite fringe interferograms.

In finite fringe interferograms, a linearly varying phase is added to the phase shifts caused by the refractive index variations. This results in straight, parallel, and equally spaced fringes in the freestream regions of the interferogram. In regions where the flow is disturbed, the fringes bend, converge, and/or diverge.

In the past, a method for determining the phase shifts involved tracing individual fringes. By measuring the displacement of individual fringes from the freestream pattern, the phase shift could be determined. The resolution of this method is limited by the fringe spacing, and it is time consuming.

By digitizing the finite fringe interferogram, gray-scale information (the intensity pattern) can be used to calculate the phase shift at every point in the interferogram. Different methods for finding the phase shift from digitized interferograms have been developed, some of them requiring multiple finite fringe interferograms[4] and others requiring a single interferogram.[3] Included here is a description of a technique that uses a single digitized interferogram and that fits sine waves to gray-scale values.

When calculating the phase shift from finite fringe interferograms, the frequency and phase of the freestream fringes first must be determined. A region of the digitized interferogram is identified
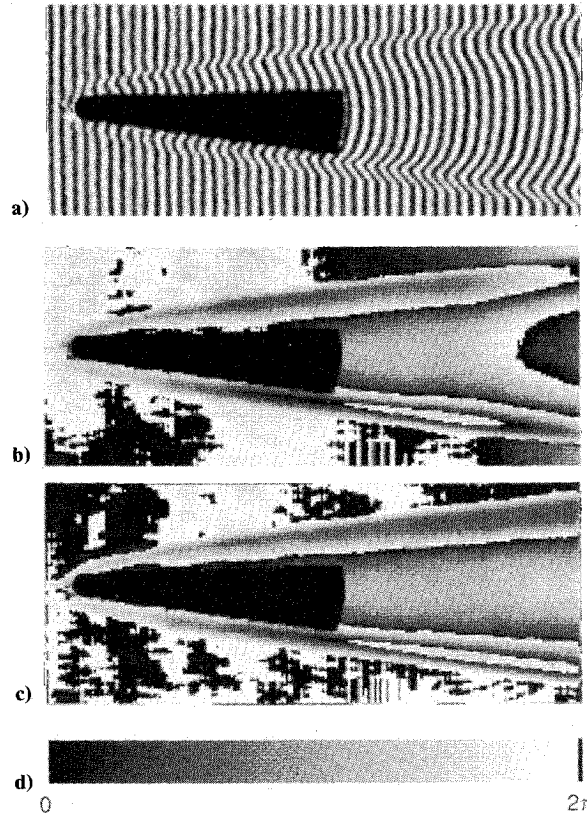

Fig. 10 Finite fringe interferogram for a blunt cone: a) experimental; b) phase shift modulo 2π; c) phase shift modulo 2π with freestream variation removed; and d) color bar.

with the freestream, and the freestream intensity pattern is approximated by

$$I_0 = A_0 + B_0 \sin(\kappa_{x_0} x + \phi_0)$$

The freestream spacing, which is determined by κ_{x_0}, and the phase ϕ_0 are found by an iterative, least-squares procedure.

Once κ_{x_0} and ϕ_0 are known, the phase shifts are determined pixel by pixel. First, a single pixel is identified in the digitized interferogram, and the gray-scale values are obtained along a line that is centered about this pixel and that is perpendicular to the freestream fringes. The length of this line is equal to one freestream wavelength. The intensity pattern is then approximated by a sinusoidal function

$$I = A + B \sin(\kappa_x x + \phi)$$

and one of three methods is used to calculate the four parameters in this equation. In the first method, κ_x is assumed to be approximately equal to κ_{x_0}, and three points that are distributed over the length of the line are used to calculate A, B, and ϕ. In the second method, the frequency is not assumed to be equal to the freestream frequency, and four points that are distributed over the length of the line are used to calculate A, B, κ_x, and ϕ. In the third method, all of the points along the line are used, and A, B, κ_x, and ϕ are found using an iterative, least-squares fitting procedure. Once κ_{x_0} and ϕ are known, the phase shift

$$\delta\phi = (\kappa_x - \kappa_{x_0})x + (\phi - \phi_0)$$

is calculated. A new pixel in the interferogram is then chosen, and the process is repeated until the phase shift is determined for every pixel in the digitized finite fringe interferogram. The differences in the calculated phase shifts using these three methods are minimal, and the first two methods are computationally much faster.

In Fig. 10a an experimental finite fringe interferogram is shown for a blunt cone. This interferogram was taken in the ballistic range

at NASA Ames Research Center. The test section pressure was 0.08 atm.[20] In Fig. 10b, the calculated phase shift modulo 2π is plotted. It should be noted that jumps from white to black represent only small changes in phase. The freestream phase shift in the majority of the lower half of Fig. 10b is white or black; hence, the calculated phase is nearly constant in this region. However, in the lower right-hand corner and in the upper half of the plot, there are variations in the calculated freestream phase shift. Investigation of the digitized image did indicate that the fringe spacing was actually varying in the freestream. Since the freestream flow in the ballistic range was uniform and quiescent, these variations are errors that have been introduced by the experimental apparatus.

The finite fringe interferogram in Fig. 10a was created using a dual plate, holographic interferometer.[20] Variations in the freestream fringe spacing could have several sources, including the spatial quality of the laser, the optics, and the reconstruction process. To remove these variations, a least-squares procedure was used to fit polynomial functions to the freestream phase. These functions were then used to correct the phase shift for the entire image, and the results are shown in Fig. 10c. In this plot, the freestream region is nearly all white and black, and the variations in the calculated freestream phase shifts are now very small. The estimated errors in the phase-shift calculations are less than 10%.

Differences in the wake regions for the uncorrected and corrected calculated phase shifts should be noted. The uncorrected phase-shift calculations indicate that there is a neck region in the wake flow. Once the freestream phase variations have been removed, the neck region disappears. Qualitative as well as quantitative analyses of finite fringe interferograms require removal of experimental errors such as those caused by optical aberrations.

Concluding Remarks

The CISS code has proven its capability in constructing interferograms, schlieren, and shadowgraphs from a variety of ideal- and real-gas, two-dimensional, axisymmetric, and three-dimensional flowfield solutions. For the examples shown here, the constructed images are very similar to the experimental images, the flow features in the constructed images are represented by the same variations in light and dark as in the experimental images. The fringe patterns in the constructed finite and infinite fringe interferograms simulate the patterns in the experimental interferograms, and one-to-one comparisons of constructed and experimental interferograms can be made. The shocks and shear layers in the constructed schlieren and shadowgraphs are defined by the same intensity variations as in their experimental counterparts. In addition, three-dimensional effects are included in the construction. Hence, one-to-one comparisons of constructed and experimental schlieren and shadowgraphs also can be made.

The quality of the flowfield solution does affect the quality of the constructed images. Insufficient or improperly placed grid points can cause spreading of shocks and shear layers in the constructed images. CISS not only provides an excellent tool for comparing flowfield solutions with experiment, but it can be also be used to identify problem areas in the flowfield solutions.

By constructing images from flowfield solutions and by comparing these images with experimental images, the ability of the flow solver to simulate experimental flows can be assessed. More detailed information for code validation can be obtained by determining phase shifts from experimental finite fringe interferograms and by comparing these phase shifts with computed phase shifts. Methods for extracting phase shifts from finite fringe interferograms do exist. It is imperative that the experimental errors caused

by optical aberrations be removed from the phase-shift calculations before either qualitative or quantitative comparisons are made. The ability to compare computations and experiments on a one-to-one basis and to extract detailed information from finite fringe interferograms is invaluable for CFD code validation.

Acknowledgment

References

[1]Dunagan, S. E., Brown, J. L., and Miles, J. B., "Interferometric Data for a Shock-Wave/Boundary-Layer Interaction," NASA TM 88227, Sept. 1986.

[2]Ben-Dor, G., Whitten, B. T., and Glass, I. I., "Evaluation of Perfect and Imperfect-Gas Interferograms by Computer," *International Journal of Heat and Fluid Flow,* Vol. 1, No. 2, 1979, pp. 77–91.

[3]Mertz, L., "Real-Time Fringe-Pattern Analysis," *Applied Optics,* Vol. 22, No. 10, 1983, pp. 1535–1539.

[4]Creath, K., "Comparison of Phase-Measurement Algorithms," *Proceedings of the SPIE 680,* Surface and Characterization and Testing, 1986, pp. 19–28.

[5]Strike, W. T., O'Hare, J. E., and Templeton, W. L., "Development of Holographic Applications in the VKF Supersonic and Hypersonic Wind Tunnels," Arnold Engineering Development Center, AEDC TR-75-1, Arnold AFB, TN, April 1975.

[6]Watkins, W., "Comparisons of a Three-Dimensional, Full Navier-Stokes Computer Model with High Mach Number Combuster Test Data," AIAA Paper 90-5217, Oct. 1990.

[7]Havener, A. G., and Obergefell, L. A., "Computational Interferometric Description of Nested Flow Fields," *Optical Engineering,* Vol. 24, No. 3, 1985, pp. 441–445.

[8]Tamura, Y., and Fujii, K., "Visualization for Computational Fluid Dynamics and the Comparison with Experiments," AIAA Paper 90-3031, Aug. 1990.

[9]Shapiro, A. H., *The Dynamics and Thermodynamics of Compressible Flow,* Vol. 1, Ronald Press Co., New York, 1953.

[10]Liepmann, H. W., and Roshko, A., *Elements of Gasdynamics,* Wiley, New York, 1957.

[11]Sharma, S. P., Ruffin, S., Meyer, S. A., Gillespie, W. D., and Yates, L. A., "Density Measurements in an Expanding Flow Using Holographic Interferometry," AIAA Paper 92-0809, Jan. 1992.

[12]Venkatapathy, E., Palmer, G., and Prabhu, D., "AFE Base Flow Computations," AIAA Paper 91-1372, June 1991.

[13]Davies, C. B., and Venkatapathy, E., "The Multi-Dimensional Self-Adaptive Grid Code, SAGE," NASA TM 103905, July 1992.

[14]Tokarcik, S., Venkatapathy, E., Candler, G., and Palmer, G., "Computational Flow Predictions for Hypersonic Drag Devices," AIAA Paper 91-3303, Sept. 1991.

[15]Delery, J., and Coet, M. C., "Experiments on Shock Wave/Boundary-Layer Interactions Produced by Two-Dimensional Ramps and Three-Dimensional Obstacles," INRIA and Societe de Mathematiques Appliques et Industrielles, Workshop on Hypersonic Flows for Reentry Problems, Antibes, France, ONERA, TP 1990-155, Jan. 1990.

[16]Ruffin, S. M., Venkatapathy, E., Lee, S. H., Keener, E. R., and Spaid, F., "Single Expansion Ramp Nozzle Simulations," AIAA Paper 92-0387, Jan. 1992.

[17]Wilson, G. J., "Computation of Steady and Unsteady Hydrogen-Air Shock-Induced Combustion over Hypervelocity Blunt Bodies," Ph.D. Dissertation, Stanford Univ., Stanford, CA, Dec. 1991.

[18]Wilson, G. J., and Sussman, M. A., "Computation of Unsteady Shock-Induced Combustion Using Logarithmic Species Conservation Equations," *AIAA Journal,* Vol. 31, No. 2, 1993, pp. 294–301.

[19]Lehr, H. F., "Experiments on Shock Induced Combustion," *Astronautica Acta,* Vol. 17, Nos. 4–5, 1972, pp. 589–597.

[20]Tam, T. C., Brock, N. J., Cavolowsky, J. A., and Yates, L. A., "Holographic Interferometry at the NASA Ames Hypersonic Free-Flight Aerodynamic Facility," AIAA Paper 91-0568, Jan. 1991.